



## Adsorptive removal of methylene blue onto $MFe_2O_4$ : kinetics and isotherm modeling

Rania Ramadan<sup>a</sup>, Nabila Shehata<sup>b,\*</sup>

<sup>a</sup>Materials Science Lab (1), Physics Department, Faculty of Science, Cairo University, Giza, Egypt, Tel. (+2) 01030899891; email: rramadan@sci.cu.edu.eg

<sup>b</sup>Faculty of Postgraduate Studies for Advance Sciences, Beni-Suef University, Beni-Suef, Egypt, Tel. +20 1119910190; email: nabila.shehata@psas.bsu.edu.eg

Received 24 January 2020; Accepted 18 March 2021

### ABSTRACT

In this study, ferrites nanoparticles of formula  $MFe_2O_4$  ( $M = Co, Zn, \text{ and } 50\% Co/50\% Zn$ ) were synthesized and characterized by X-ray diffraction, Fourier transforms infrared spectroscopy, scanning electron microscopy, energy-dispersive X-ray spectroscopy, and the  $N_2$  adsorption–desorption technique. The magnetic properties were studied using a vibration sample magnetometer, and the magnetic susceptibility was measured as a function of temperature. Among the specimens evaluated,  $CoFe_2O_4$  has the largest saturation magnetization (66.380 emu/g), and  $ZnFe_2O_4$  exhibits the largest surface area (120.1  $m^2/g$ ). The prepared nanoparticles were investigated as adsorbents for the removal of methylene blue (MB) from an aqueous solution at different contact times, pH, and initial concentrations. The influence of the adsorption conditions was examined, finding that the adsorption process is favored in alkali conditions and high MB concentration. The Langmuir and Freundlich models fit the adsorption data of  $CoFe_2O_4$  and the composite, whereas only the Freundlich model fits the experimental results of  $ZnFe_2O_4$ . The adsorption kinetics of MB adsorption onto  $MFe_2O_4$  is better described by pseudo-first-order and pseudo-second-order models than by an intraparticle diffusion model.

**Keywords:** Ferrites nanoparticles;  $CoFe_2O_4$ ;  $ZnFe_2O_4$ ; Nanocomposite; Methylene blue

### 1. Introduction

Industrial development is continuously increasing, and with it, the amount of wastewater discharged to the environment. This wastewater contains a large amount of pollutants, predominantly dyes, which are used and discharged in different industries like painting, paper, and textiles, with a negative impact on nature, aquatic plants, and animals [1]. Consequently, many research efforts have been devoted to the removal of dyes from wastewater. Among the dyes investigated, adsorption stands out because it is a low-cost process. Nowadays, research attention

in this field is mainly focused on the development of innovative nanomaterials as new adsorbents.

Recently, nanoparticles have attracted attention for wastewater management owing to their excellent adsorptive characteristics resulting from their high surface area and specific mechanical and chemical properties [2]. In adsorption studies, methylene blue (MB) is widely used as a model dye, and its adsorption from water has been investigated using different adsorbents such as activated lignin–chitosan extruded pellets [3], a  $Fe_3O_4@AMCA-MIL-53(Al)$  nanocomposite [4], and arginine-modified activated carbon [5]. In this context, the adsorption technique has also been favored because of its low

\* Corresponding author.

cost, rapidity [6], and applicability to the efficient removal of water pollutants using adsorbents based on industrial by-products [7].

Ferrite nanoparticles are an interesting class of nanoparticles. Some studies have investigated the modification of magnetic ferrite nanoparticles; however, their applications are scarcely reported because of their low surface area and high tendency to oxidize. For example, Rahimi et al. [8] investigated  $\text{ZnFe}_2\text{O}_4$  prepared by a solvothermal method for the removal of Congo red (CR) from wastewater, for which the maximum adsorption capacity ( $q_{\text{max}}$ ) was 16.6 mg/g. Etemadinia et al. [9] examined a nanocomposite based on  $\text{ZnFe}_2\text{O}_4$  for the removal of MB, achieving a  $q_{\text{max}}$  of 109.37 mg/g at pH 8. Another adsorbent based on  $\text{ZnFe}_2\text{O}_4$  was developed by Hou et al. [10] using a sol-gel method. The samples showed high adsorption capacity (>90%). They concluded that the adsorption capacity toward MB increased with the Zn substitution in the composite, whereas the quickest adsorption occurred at the lowest substitution value. Li et al. [11] synthesized  $\text{ZnFe}_2\text{O}_4$  using a facile biotemplate method and tested it for the removal of acid fuchsin. Konicki et al. [12] employed a microwave/hydrothermal method to synthesize  $\text{ZnFe}_2\text{O}_4$ , which was characterized and studied for the removal of acid dye (AR88). The effects of various parameters such as initial concentration, pH solution, and temperature were investigated. Feng et al. [13] synthesized  $\text{ZnO@ZnFe}_2\text{O}_4$  using a microwave combustion technique. The surface area and MB removal efficiency from the aqueous solution were found to increase with the fuel mass, and the  $q_{\text{max}}$  reached 37.27 mg/g within 0.5 min. Liang et al. [14] prepared  $\text{CoFe}_2\text{O}_4$ @activated carbon for the removal of gentian violet and investigated the adsorption parameters. The  $q_{\text{max}}$  was 184.2 mg/g. The same adsorbent was investigated for the removal of MB [15], reaching a removal efficiency of 99%. Tatarchuk et al. [16] synthesized Co-Zn $\text{Fe}_2\text{O}_4$  for the removal of two dyes (cationic and anionic). They found that the removal efficiency toward MB increased as the Co percentage in the composite increased. In contrast, the removal efficiency of the composite for acid orange 7 increased with the zinc percentage in the composite. Ai et al. [17] modified  $\text{CoFe}_2\text{O}_4$  for dye removal using montmorillonite. The resulting adsorbent was characterized and investigated for the removal of MB, achieving a  $q_{\text{max}}$  of 97.75 mg/g. Samoila et al. [18] developed  $\text{CoFe}_2\text{O}_4$  using a sol-gel auto combustion method. The  $q_{\text{max}}$  toward CR was 14.06 mg/g at 293 K. Ding et al. [19] studied the effect of the ethanol percentage during the synthesis of  $\text{CoFe}_2\text{O}_4$  using a hydrothermal approach. It was found that the ethanol percentage affected the Brunauer-Emmett-Teller (BET) surface area and the pore structure. A  $q_{\text{max}}$  of 190.5 mg/g was obtained for an ethanol/water volume ratio of 4/3. Zhao et al. [20] enhanced the adsorptivity of  $\text{CoFe}_2\text{O}_4$  toward CR by doping with gadolinium. The removal efficiency increased by 18.6% compared with that of undoped  $\text{CoFe}_2\text{O}_4$ , and a  $q_{\text{max}}$  of 263.2 mg/g was reached. Yavari et al. [21] functionalized  $\text{CoFe}_2\text{O}_4$  with amine groups, and the developed adsorbent was investigated for the removal of three anionic dyes (DR80, DC6, and AB92). The obtained adsorbents were characterized

by Fourier transform infrared (FTIR) spectroscopy, X-ray diffraction (XRD), specific surface area, and zeta potential. Different adsorption parameters were also studied. Jacob et al. [22] suggested alternatives to activated carbon for water purification. They investigated a fixed bed based on  $\text{CoFe}_2\text{O}_4$  for the removal of cationic (MB and malachite green) and anionic dyes (Orange G and CR) and their mixtures, finding that the adsorption mechanism was based on film diffusion. Li et al. [23] functionalized  $\text{CoFe}_2\text{O}_4$  with graphene sheets, which exhibited a  $q_{\text{max}}$  of 71.5 mg/g for the removal of methyl orange from an aqueous solution.

Oyetade et al. [24] compared  $\text{CoFe}_2\text{O}_4$  and carbon nanotube-cobalt ferrite nanocomposites for the removal of rhodamine B from aqueous solution in terms of pH, contact time, adsorbent dose, dye concentration, and temperature. The composite exhibited higher adsorption capacity. Wang et al. [25] investigated the removal of CR using  $\text{CoFe}_2\text{O}_4$  synthesized by hydrothermal technique. Interestingly, they found that the adsorption capacity depended mainly on the cations distribution on the ferrite nanoparticles and that electrostatic adsorption governed the adsorption mechanism. In addition, acetone was an effective reagent for the regeneration of the spent adsorbent. The  $q_{\text{max}}$  was 244.5 mg/g.

Compared with the adsorption of MB onto ferrite materials in previous studies (Table 1), the adsorbents evaluated in the present study showed low adsorption capacities because of their low specific surface area. However, their efficiencies were enhanced by introducing specific functional groups to their surface. Moreover, it is known that the internal surface area and porosity of the ferromagnetic materials can be increased by decreasing the annealing temperature during their synthesis.

Bearing this in mind, the adsorptive behavior of MB onto Co/Zn ferrites was reported [16]. However, the researchers focused on the effect of Co/Zn on the adsorptivity of MB. Herein, we investigated the microstructural behavior and morphological and magnetic characteristics of  $\text{MFe}_2\text{O}_4$ , where M is Co, Zn, and Co/Zn, to explore the adsorption mechanisms. The three adsorbents were characterized by XRD, FTIR, scanning electron microscopy (SEM), energy-dispersive X-ray spectroscopy (EDX), and surface area analysis. The magnetic properties were studied using a vibration sample magnetometer (VSM), and the magnetic susceptibility was measured as a function of temperature. The adsorptive removal of MB was evaluated by varying the pH, initial MB concentration, and contact time.

## 2. Experimental

### 2.1. Materials

All chemicals of analytical grade were used to prepare the samples.  $\text{Fe}(\text{NO}_3)_3$ ,  $\text{Co}(\text{NO}_3)_2$ ,  $\text{Zn}(\text{NO}_3)_2$ , and urea were purchased from Sigma-Aldrich (Germany) with a purity of 99.9%. A stock solution of MB was prepared by dissolving 1 g of MB in 1 L of distilled water. This stock solution was diluted as needed for the adsorption studies using distilled water.

## 2.2. Preparation of ferrites nanoparticles

Cobalt-ferrite,  $\text{CoFe}_2\text{O}_4$ , nanoparticles were prepared as shown in Fig. 1. Briefly,  $\text{Fe}(\text{NO}_3)_3 \cdot 9\text{H}_2\text{O}$ ,  $\text{Co}(\text{NO}_3)_2 \cdot 6\text{H}_2\text{O}$ , and urea were burned together and then grinded, followed by sintering at  $900^\circ\text{C}$  for 2 h. Finally, the product was grinded again for 1 h.  $\text{ZnFe}_2\text{O}_4$  nanoparticles were prepared following the same procedure by replacing  $\text{Co}(\text{NO}_3)_2$  with  $\text{Zn}(\text{NO}_3)_2$ . The nanocomposites (50%  $\text{CoFe}_2\text{O}_4$ /50%  $\text{ZnFe}_2\text{O}_4$ ) were prepared by grinding method.

## 2.3. Characterization

The samples were characterized by XRD (Poker D8 Advance) in a Bragg angle range of  $20^\circ \leq 2\theta \leq 80^\circ$ . The crystallite size (Table 2) was calculated by using the following Debye–Scherrer equation [29]:

$$D = \frac{0.9\lambda}{\beta \cos \theta} \quad (1)$$

where  $\lambda$  is the X-ray wavelength,  $\beta$  is the full width at half maximum intensity, and  $\theta$  is the Bragg angle.

The morphology and surface of the samples were characterized by field-emission SEM (FESEM). A VSM model 9600-1 LDJ, USA, and Faraday's method with a homemade setup were used to study the magnetic properties and to measure the magnetic susceptibility as a function of the absolute temperature at different magnetic field intensities, respectively.

The specific surface area can be calculated using MB [30] according to Eq. (2) as follows:

$$S_{\text{mb}} = \frac{F \times q_{\text{max}} \times N \times A}{M} \quad (2)$$

where  $S_{\text{mb}}$  is the specific surface area using MB test ( $\text{m}^2/\text{g}$ ),  $F$  is the purity of MB (-),  $q_{\text{max}}$  is the maximum adsorption capacity of MB onto  $\text{MFe}_2\text{O}_4$  ( $\text{mg}/\text{g}$ ),  $A$  is the cross-section area of one molecule of MB ( $\text{\AA}^2$ ),  $N$  is Avogadro's number ( $6.023 \times 10^{23} \text{ mol}^{-1}$ ), and  $M$  is the molecular weight of MB ( $355.89 \text{ g}/\text{mol}$ ).

## 2.4. Adsorption experiments

To investigate the adsorption of MB onto  $\text{MFe}_2\text{O}_4$ , 0.1 g of adsorbent and 100 mL of MB were mixed together in the dark. The effect of pH (2–10) was determined by adding drops of NaOH or HCl (0.1 N) as required. The effect of the initial MB concentration (10–100 mg/L) on the adsorption properties was also investigated. The adsorption isotherm was determined by subtracting the amount of dye that remained in the solution ( $C_t$ ) from the initial dye concentration ( $C_0$ ) multiplied by the volume of the solution (L) divided by the amount of adsorbent (g). The initial and final concentrations of MB were analyzed by ultraviolet-visible (UV-vis) spectroscopy at a wavelength of 655 nm. The adsorption capacity,  $q_t$ , was calculated according to the following equation [31]:

Table 1  
Maximum removal capacities of methylene blue ions using  $\text{MFe}_2\text{O}_4$  and their derivatives under different conditions

Adsorbent based on $\text{MFe}_2\text{O}_4$	$q_{\text{max}}$ (mg/g)	pH	$C_0$ (mg/L)	Time (min)	Ref.
$\text{ZnFe}_2\text{O}_4 @ \text{SiO}_2 @ \text{Tragacanth gum}$	109.4	8	60	60	[9]
$\text{SDS} @ \text{ZnFe}_2\text{O}_4$	699.30	12	40–100	150	[26]
$\text{ZnO} @ \text{ZnFe}_2\text{O}_4$	37.27	7	5–100		[13]
$\text{Mn}_{1-x}\text{Zn}_x\text{Fe}_2\text{O}_4$	40.97	9–10	7.5–100	180	[10]
$\text{CoFe}_2\text{O}_4 @ \text{Co}_x\text{Fe}_y @ \text{AC}$	196.7	–	250	50	[27]
Montmorillonite@ $\text{CoFe}_2\text{O}_4$	97.75	–	40–20	–	[17]
$\text{CoFe}_2\text{O}_4$	0.86–3.37	7	10–150	–	[28]
$\text{CoZn} @ \text{Fe}_2\text{O}_4$	3.4				[16]
$\text{ZnFe}_2\text{O}_4$	3.6	7	10–100	240	This study
$\text{CoFe}_2\text{O}_4$	1.91				
50% $4\text{CoFe}_2\text{O}_4$ + 50% $\text{ZnFe}_2\text{O}_4$	3.88				

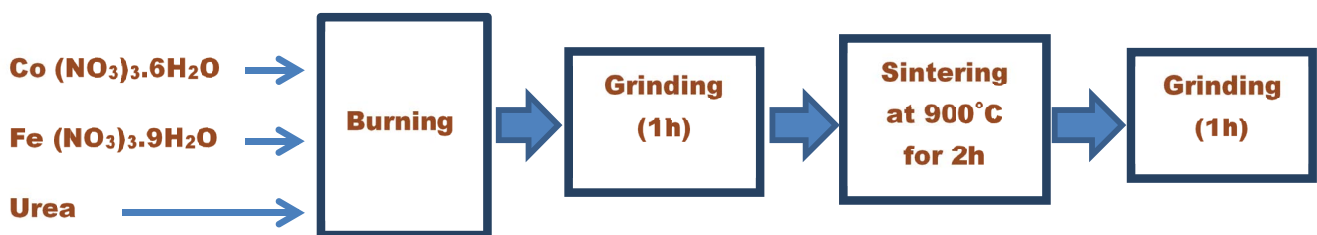


Fig. 1. Preparation technique for  $\text{ZnFe}_2\text{O}_4$  and  $\text{CoFe}_2\text{O}_4$  nanoparticles and the 50%  $\text{CoFe}_2\text{O}_4$ /50%  $\text{ZnFe}_2\text{O}_4$  nanocomposite.

$$q_e = \frac{(C_0 - C_f)V}{m} \tag{3}$$

2.5. Adsorption isotherms

The Langmuir [32], Freundlich [33], and Langmuir–Freundlich models [34] were used to calculate the parameters of MB adsorption onto  $MFe_2O_4$ . The linearizing form of Langmuir and Freundlich expressions are represented by Eqs. (4) and (5), respectively, and the nonlinear equation of the Langmuir–Freundlich model can be described by Eq. (6):

$$\frac{C_e}{q_e} = \frac{a_L}{K_L} C_e + \frac{1}{K_L} \tag{4}$$

$$\log q_e = \log K_F + \frac{1}{n} \log C_e \tag{5}$$

$$q_e = \frac{q_{MLF} (K_{LF} C_e)^{MLF}}{1 + (K_{LF} C_e)^{MLF}} \tag{6}$$

where  $a_L$  and  $K_L$  are Langmuir constants,  $K_F$  and  $n$  are Freundlich constants,  $q_{MLF}$  is the Langmuir–Freundlich maximum adsorption capacity (mg/g),  $K_{LF}$  is the equilibrium constant for a heterogeneous solid, and  $M_{LF}$  is a heterogeneous parameter that lies between 0 and 1. The equilibrium coefficients were calculated from the equation  $R_L = 1/(1 + K_L C_0)$ .

2.6. Adsorption kinetics

The adsorption kinetics values were determined according to the adsorption studies of 0.1 g of  $MFe_2O_4$  in MB solutions of different concentrations (10, 30, and 50 mg/L) at room temperature. The concentration of MB in the supernatant solution was determined by UV-vis analysis. To study the adsorption kinetic mechanism, the following three models were applied:

Pseudo-first-order model [35]:

$$\ln(q_e - q_t) = \ln q_e - k_1 t \tag{7}$$

Pseudo-second-order model [36]:

$$\frac{t}{q_t} = \frac{1}{k_2 q_e^2} + \frac{t}{q_e} \tag{8}$$

Intraparticle diffusion model [37]:

$$q_t = k_{ip} \sqrt{t} + c_{ip} \tag{9}$$

where  $k_1$  and  $k_2$  are the pseudo-first- and pseudo-second-order rate constants ( $\text{min}^{-1}$  and  $\text{g/mg min}$ , respectively),  $k$  is the diffusion coefficient ( $\text{mg/g min}^{0.5}$ ), and  $c_{ip}$  is the intraparticle diffusion constant (mg/g).

To determine the model that provided a better fit of the experimental data, each model was evaluated in terms of the difference between the calculated and experimental adsorption capacity values and the correlation coefficient ( $R^2$ ) obtained.

3. Results and discussion

3.1. Characterization of the adsorbents

3.1.1. XRD analysis.

Fig. 2 shows the XRD diffraction patterns of the prepared samples. The presence of the reflection planes (220),

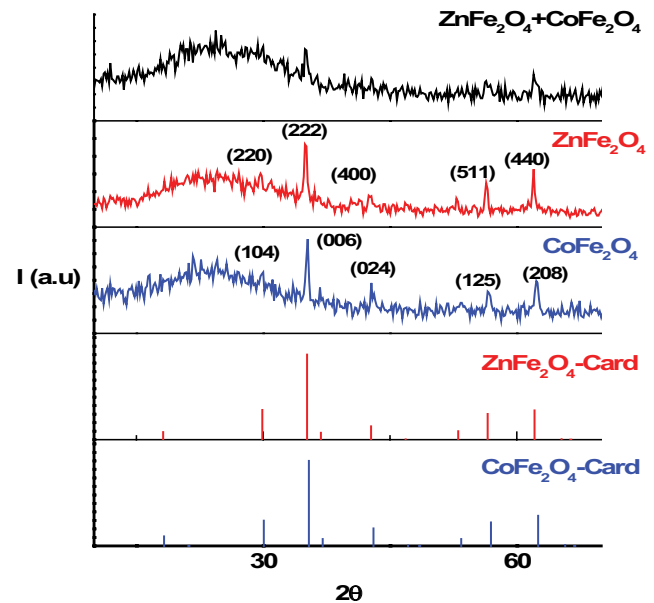


Fig. 2. X-ray diffraction patterns of  $MFe_2O_4$ .

Table 2

Comparison between theoretical and experimental values of lattice parameters ( $a$ ,  $b$ , and  $c$ ), cell volume ( $V$ ), and crystallite size ( $D$ )

Sample	Theoretical values			Experimental values			
	$A$ (Å)	$C$ (Å)	$V$ (Å) <sup>3</sup>	$A$ (Å)	$C$ (Å)	$V$ (Å) <sup>3</sup>	$D$ (nm)
$CoFe_2O_4$	5.9366	14.543	443.87	5.9367	14.543	443.89	10
$ZnFe_2O_4$	8.4465	8.4465	602.60	8.4464	8.4464	602.58	8
50% Zn/50% $CoFe_2O_4$							12

(222), (400), (511), (440), (104), (006), (024), (125), and (208) indicates the pure formation and crystallinity of  $MFe_2O_4$ . Table 2 summarizes a comparison of the experimental values of the lattice parameters  $a$ ,  $b$ , and  $c$  and the volume of the unit cell with the theoretical values of the ICDD cards 01-079-1744 for  $CoFe_2O_4$  and 01-079-1150 for  $ZnFe_2O_4$  for all the samples. A good agreement between experimental and theoretical values can be observed.

Table 2 clarifies the agreement between experimentally calculated values and theoretical ones obtained from ICDD.

### 3.1.2. Magnetic properties of $MFe_2O_4$

To investigate the magnetic behavior of the prepared samples, the magnetic hysteresis loops were studied at room temperature. As shown in Fig. 3, the saturation magnetization of  $CoFe_2O_4$ ,  $ZnFe_2O_4$ , and 50% Zn/50%  $CoFe_2O_4$  was 66.380, 2.7327, and 35.545, respectively.  $CoFe_2O_4$  has ferromagnetic properties with high saturation magnetization and coercivity, which are related to the high ordered spin arrangement of spinel  $CoFe_2O_4$  [38,39]. For a normal spinel structure of bulk  $ZnFe_2O_4$ ,  $Zn^{2+}$  (nonmagnetic) occupies the A position, and  $Fe^{3+}$  (magnetic) occupies the B position; owing to the absence of A–B superexchange interaction, bulk  $ZnFe_2O_4$  would not show any magnetic behavior theoretically. When  $ZnFe_2O_4$  is prepared in the nanoscale, a small portion of nonmagnetic  $Zn^{2+}$  occupies B sites, and some  $Fe^{3+}$  occupies A sites. This A–B exchange explains the transformation of the magnetic behavior of  $ZnFe_2O_4$  from paramagnetic to weakly ferromagnetic with a very small value of the saturation magnetization [40]. The present

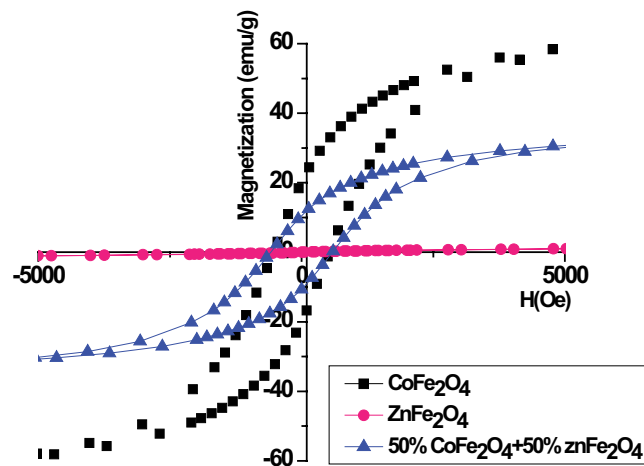


Fig. 3. Magnetic hysteresis loops of the  $MFe_2O_4$  samples ( $M = Co$ ,  $Zn$ , and 50%  $Zn/50\% Co$ ).

Table 3  
Magnetic parameters of  $MFe_2O_4$

Samples	$M_s$ (emu/g)	$M_r$ (emu/g)	Positive $H_c$ (G)	Negative $H_c$ (G)	$M$ – $H$ loop area (erg/g)
$CoFe_2O_4$	66.380	19.890	529.27	–533.27	$125.84 \times 10^3$
$ZnFe_2O_4$	2.7327	$8.3292 \times 10^{-3}$	16.628	–14.084	793.38
50% $CoFe_2O_4$ + 50% $ZnFe_2O_4$	35.545	10.584	582.57	–585.00	$69.344 \times 10^3$

composite sample showed intermediate magnetic behavior because of the mixing of strongly and weak magnetic materials. Table 3 shows the magnetic parameters of the prepared samples, which range from low to high values.

### 3.1.3. Molar magnetic susceptibility as a function of temperature at different field intensities.

All samples represented in Figs. 4a–c follow the same trend. At low temperatures, the molar magnetic susceptibility ( $\chi_M$ ) has a constant value because the temperature is not sufficiently high to align the magnetic moments. Then, a gradual decrease is observed with increasing temperature until a certain temperature (Curie temperature). After that,  $\chi_M$  decreases drastically as the temperature keeps rising, and the material loses its ferromagnetic properties. At a temperature equal or above the Curie temperature, the magnetocrystalline anisotropy disappears, which is related to the drop of magnetization. Subsequently, the samples reach paramagnetic behavior with a completely disordered state. As shown in Figs. 4a–c, an increase in the field intensities is accompanied by a decrease in  $\chi_M$  for all the samples, which can be explained by the following equation:

$$\chi_M = \frac{M}{H} \quad (10)$$

where  $M$  is the magnetization and  $H$  is the field intensity. By increasing the field intensity, the spin magnetic moment alignment increases until reaching saturation values, and the magnetization reaches a constant value. This leads to a decrease in  $\chi_M$  with any increase in the field intensities.

## 3.2. Adsorption studies of methylene blue onto ferrite nanoparticles

### 3.2.1. Effect of pH

The pH of the solution affects the adsorbate characteristics in the solution, the surface charge of adsorbents, and the adsorption mechanism [41,42]. As shown in Fig. 5, the adsorption capacities increase slightly with increasing pH from 2 to 9, followed by a sharp increase from pH 9 to 11. This may be attributed to the fact that the affinity of  $MFe_2O_4$  toward the cationic MB dye increases at higher pH to compensate for the positive charge of the dye molecules. Zeta potentials of  $ZnFe_2O_4$ ,  $CoFe_2O_4$ , and 50%  $CoFe_2O_4/50\% ZnFe_2O_4$  were positively charged. The surface of the adsorbent subjected to protonation/deprotonation is dependent on the pH solution. The net surface charge at pH lower than these values is positive, which is not preferable for adsorbing the cationic MB species. An

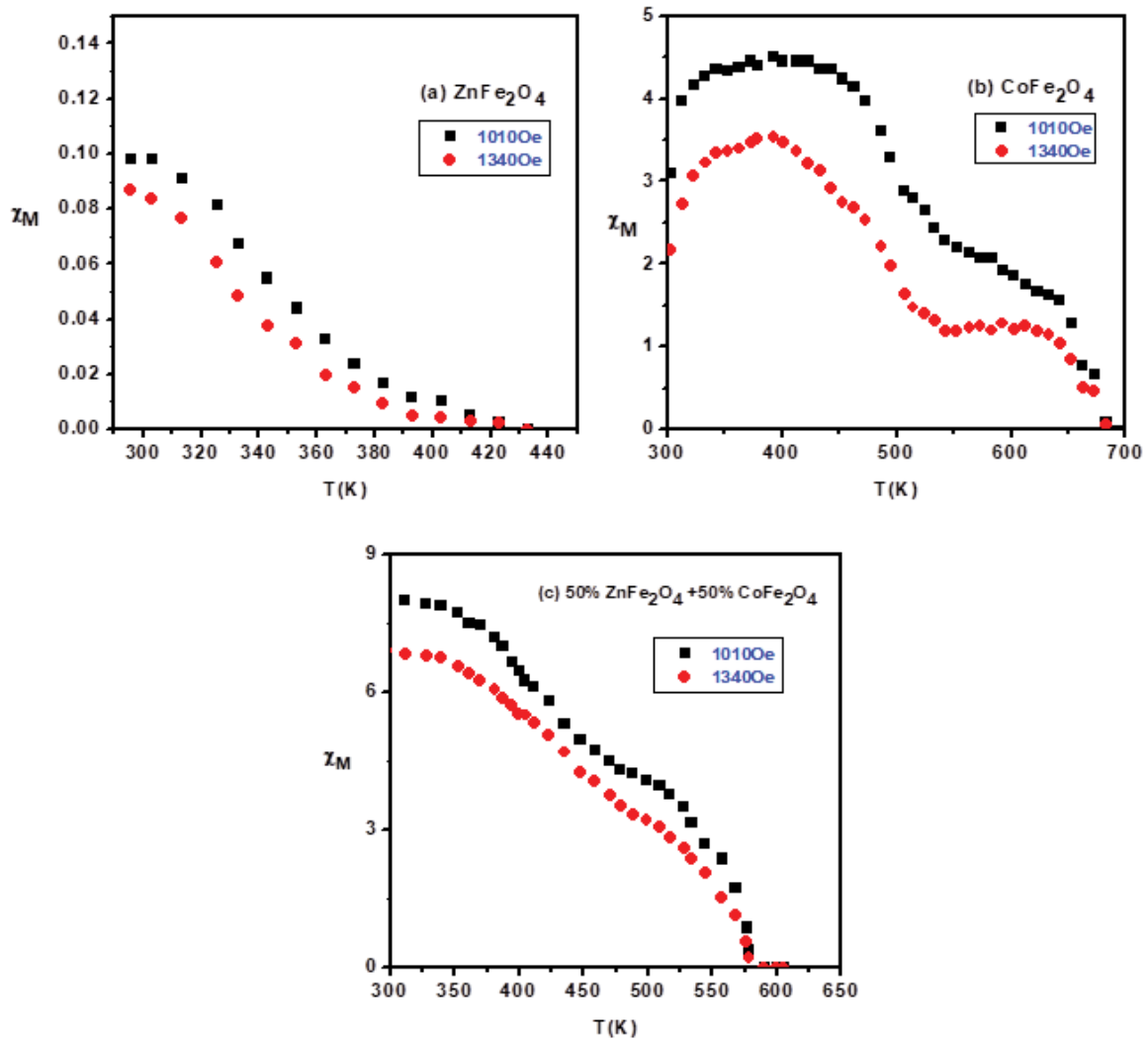


Fig. 4. Molar magnetic susceptibility as a function of temperature at different field intensities for: (a)  $CoFe_2O_4$ , (b)  $ZnFe_2O_4$ , and (c) 50%  $CoFe_2O_4$ /50%  $ZnFe_2O_4$ .

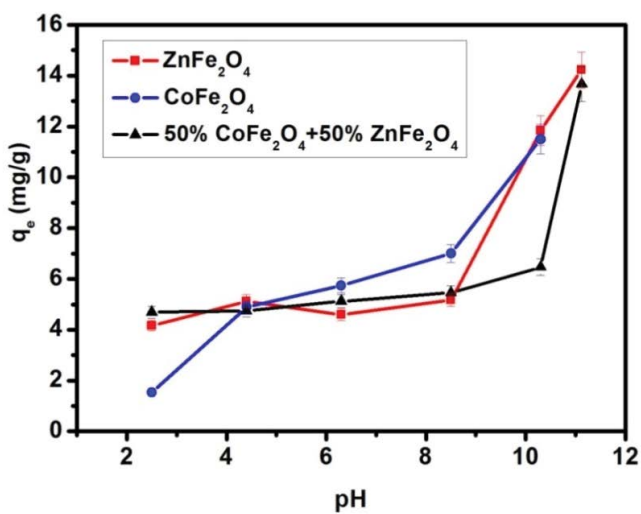


Fig. 5. Effect of pH on the adsorption of methylene blue onto  $MFe_2O_4$  ( $V = 50$  mL,  $m = 0.1$  g,  $C_0 = 50$  mg/L, and  $t = 4$  h).

increase in pH resulted in a build-up of negative charges on both adsorbent and adsorbate, leading to an enhanced electric attraction between them. The ferrite nanoparticles have positive charges on their surfaces because of the presence of  $Zn^{2+}$  and  $Co^{2+}$ , resulting in partial repulsion with the cationic MB dye. Generally, at high pH, the presence of OH anions decreases these repulsion forces and enhances the electrostatic attraction between MB and  $MFe_2O_4$  [12,43]. The  $p_{ka}$  of MB is 3.8 [44], resulting in a net positive charge in the surface of the dye molecule that explains the low adsorption capacity and affinity at low pH.

### 3.2.2. Adsorption isotherm

The adsorption capacities of MB onto the magnetic ferrite nanoparticles ( $MFe_2O_4$ ) at equilibrium vs. equilibrium MB concentration are shown in Fig. 6. According to Gils classification, all of them are isotherms of type L3, which indicates the flat orientation of the MB molecule onto  $MFe_2O_4$ . The isotherm profile also suggests the accumulation of MB

molecules in the form of layers on the surface of  $MFe_2O_4$ . As the concentration increases, the attraction of the magnetic nanoparticles toward MB increases. The adsorbents under study show high surface area and low adsorption capacity, which may be attributed to the agglomeration of the magnetic particles [26]. This could be also explained in terms of the effect of the microstructure, pore-volume, and distribution and surface morphology of these materials on their adsorption capacity, despite exhibiting large surface area [19]. As can be seen from Fig. 6, the difference in the size of Zn and Co ferrite nanoparticles leads to compacting of the resulted composite, in which small particles are embedded in the space and pores of larger particles. The synthesis procedure for magnetic ferrite is known to play an important role in the adsorption mechanism and capacity [45–47]. Thus, for adsorption purposes, higher pore volume and better pore shape and size are obtained at lower temperatures; the annealing temperature should not exceed  $400^\circ\text{C}$  [48,49]. The introduction of functional

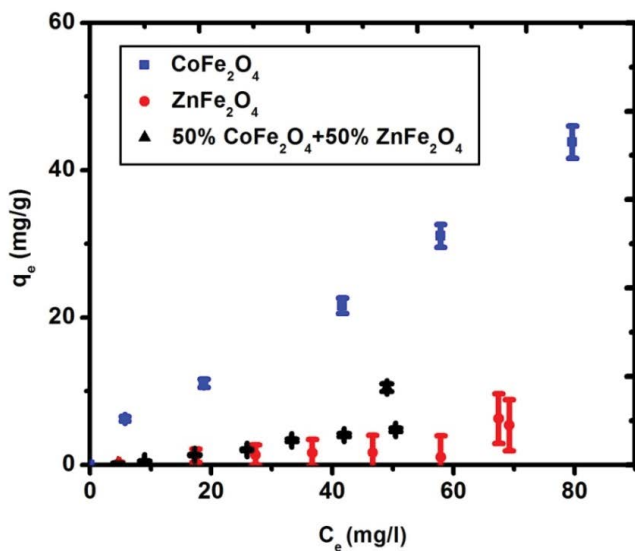


Fig. 6. Sorption of methylene blue onto  $MFe_2O_4$  at  $25^\circ\text{C}$ ,  $m = 0.05$  g.

groups on the surface of the ferrite nanoparticles has been suggested for the removal of specific pollutants.

According to the results summarized in Table 4, the Langmuir and Freundlich models fit the data obtained for  $CoFe_2O_4$ , whereas only the Freundlich model fits the experimental results of  $ZnFe_2O_4$ . For the composite, both models fit the experimental data, but the correlation coefficient of the Freundlich model is higher than that of the Langmuir model. In contrast, the Langmuir–Freundlich model does not fit the experimental data. For the MB adsorption onto  $MFe_2O_4$ , the values of the equilibrium parameter  $R_L$  are less than 1, ranging from 0.012 to 0.67, which confirms the favorable adsorption.

### 3.2.3. Effect of initial MB concentration and contact time

The effect of contact time and initial concentration of MB on its adsorption onto  $MFe_2O_4$  was investigated (Fig. 7). It was found that the adsorption capacity increased with both the initial MB concentration and the contact time. The adsorption capacity of  $MFe_2O_4$  reached equilibrium very fast (30 min) at low MB concentration (10–30 mg/L), whereas the time to reach equilibrium increased to 120 min at higher concentration (50 mg/L). This may be attributed to the increased competition of MB molecules for the adsorption sites on  $MFe_2O_4$  as the concentration increases. Another reason could be the presence of MB molecules in dimer form at higher concentrations; the surface area of the monomer molecule is  $130 \text{ \AA}$ , which is relatively higher than the pore of the adsorbent (13.9–14.7 nm). However, as the concentration of MB molecules increases in the same volume of the solution, the repulsion between the charges on the adsorbates slows down the adsorption rate. Overall, it can be concluded that both the initial MB concentration and the contact time play an important role in the adsorption of MB onto  $MFe_2O_4$ .

### 3.2.4. Adsorption kinetics

The kinetic parameters of pseudo-first- and pseudo-second-order models were determined from the linear plots of  $\ln(q_e - q_t)$  and  $t/q_t$  vs.  $t$ , respectively (Figs. S1 and S2).

Table 4  
Parameters of the Langmuir, Freundlich, and Langmuir–Freundlich models

Adsorption models	Parameter	$ZnFe_2O_4$	$CoFe_2O_4$	50% $CoFe_2O_4$ /50% $ZnFe_2O_4$
Langmuir	$q_{\max}$ (mg/g)	3.64	1.91	3.88
	$K_L$ (L/mg)	0.075	0.857	0.05
	$a_L$ (L/mg)	0.021	0.45	0.013
	$R^2$	0.11	0.99	0.79
Freundlich	$K_F$ (mg/g)	0.047	1.52	0.015
	$n_f$	1.047	0.737	1.544
	$R^2$	0.67	0.97	0.83
Langmuir–Freundlich	$q_{\max}$ (mg/g)	9,378	46	52,610
	$K_{LF}$ (L/mg)	0.002	0.009	1E-05
	$M_{LF}$	2.059	3.75	1.018
	$R^2$	0.87	0.88	0.99

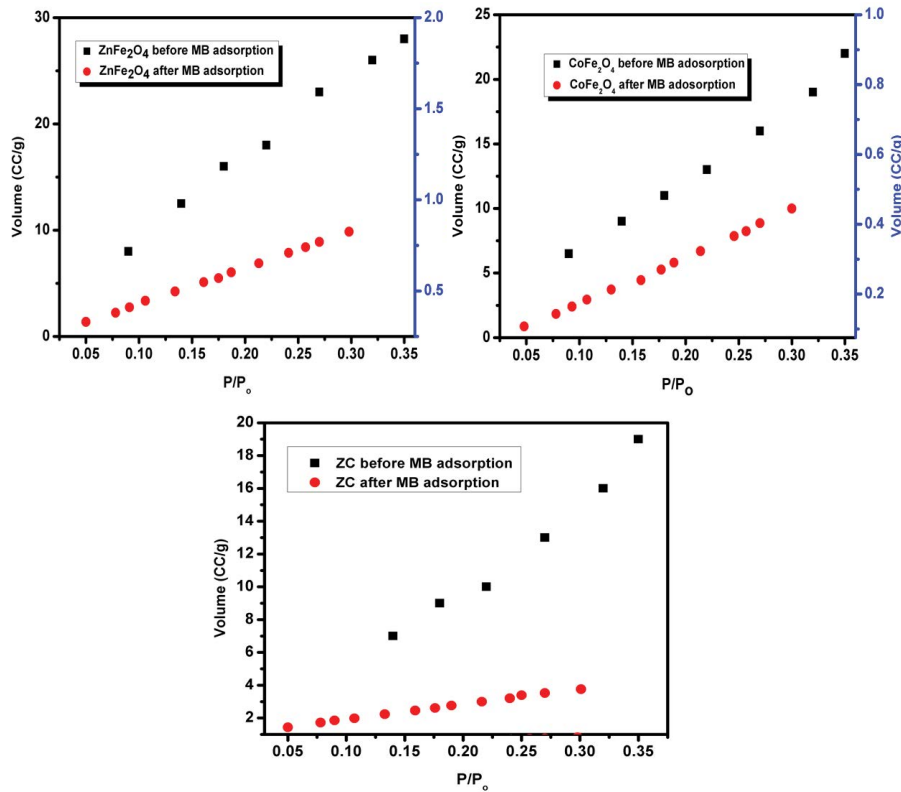


Fig. 7. Brunauer–Emmett–Teller plot of  $MFe_2O_4$  samples before and after methylene blue adsorption.

Table 5

Kinetic parameters (pseudo-first- and pseudo-second-order and intraparticle diffusion models) for the adsorption of methylene blue onto  $MFe_2O_4$

	$C_0$ (mg/L)	$q_{exp}$ (mg/g)	Pseudo-first-order model			Pseudo-second-order model		
			$k_1$ ( $min^{-1}$ )	$q_{cal}$ (mg/g)	$R^2$	$k_2$ (g/mg min)	$q_{cal}$ (mg/g)	$R^2$
$ZnFe_2O_4$	10	3.78	0.0013	10.1	0.13	0.11	3.94	0.99
	30	11.52	0.0034	1.18	0.08	0.12	11.51	0.99
	50	17.9	0.0057	3.7	0.43	0.021	17.86	0.99
$CoFe_2O_4$	10	3.8	0.004	3.2	0.09	0.0718	3.73	0.99
	30	8.7	0.0073	1.05	0.4	0.0137	8.53	0.99
	50	16.4	0.0044	2.2	0.22	0.0037	16.34	0.99
50% $CoFe_2O_4$ /50% $ZnFe_2O_4$	10	3.8	0.0021	4.16	0.02	0.483	3.834	0.99
$ZnFe_2O_4$	30	9.12	0.003	2.73	0.06	0.715	9.124	1
	50	17.3	0.0044	3.4	0.42	0.0141	17.73	0.99
	$C_0$ (mg/L)	$q_{exp}$ (mg/g)	Intraparticle diffusion model					
			$k_{ip}$	$c_{ip}$	$R^2$			
$ZnFe_2O_4$	10	3.78	0.24	0.62	0.78			
	30	11.5	0.72	1.65	0.81			
	50	17.9	1.09	2.37	0.83			
$CoFe_2O_4$	10	3.8	0.23	0.61	0.78			
	30	8.7	0.52	1.44	0.77			
	50	16.4	1.01	2.43	0.81			
50% $CoFe_2O_4$ + 50% $ZnFe_2O_4$	10	3.8	0.24	0.62	0.78			
	30	9.12	0.56	1.5	0.78			
	50	17.3	1.07	2.34	0.83			

The resulting parameters of the models are summarized in Table 5 and Fig. S4. The correlation coefficients for the pseudo-second-order model were very high (0.99–1) compared with those for the pseudo-first-order model (0.02–0.43), which suggests that the adsorption process obeys a pseudo-second-order model. The experimental data also agreed with the latter, which confirms that the adsorption process is better described by a pseudo-second-order model. All these results suggest that the rate-limiting step of the adsorption of MB onto  $MFe_2O_4$  might be chemical adsorption.

The kinetic parameters of the intraparticle diffusion model were determined from the plots of  $q_t$  vs.  $t$  (Fig. S3). The calculated parameters of the model are summarized in Table 5, which shows that the experimental data were fitted to the model with good correlation coefficients.

### 3.3. Determination of the specific surface area using MB

Monomer or dimer form hinders the calculation of the cross-section area, which might be also complicated by the different orientations that the MB molecules can adopt on the adsorbent, that is, lying flat on the adsorbent surface, sandwiched in the adsorbent pores, or adsorbed perpendicular to the surface. The dimensions of the MB molecule are  $17 \text{ \AA} \times 7.6 \text{ \AA} \times 3.25 \text{ \AA}$ . However, the adsorption isotherm profile suggests the presence of multilayers (Fig. 6), resulting in the adsorption of the MB molecules as monomers lying flat to the adsorbent surface. Thus, the cross-section area of the MB molecule ( $A$ ) can be estimated to be  $129 \text{ \AA}^2$  ( $17 \text{ \AA} \times 7.6 \text{ \AA}$ ). Table 6 summarizes the values of  $S_{mb}$  obtained by inserting the following values in Eq. (2):  $F = 0.70$ ,  $N = 6.023 \times 10^{23} \text{ (mol}^{-1}\text{)}$ , and  $M = 319.86 \text{ g/mol}$ .

### 3.4. Adsorption mechanism

#### 3.4.1. Surface area analysis using BET

According to the data in Fig. 7, all samples exhibit type IV isotherms, which are related to mesoporous structures [50]. The pore volume, pore diameter, and specific surface area were determined, and the results are listed in Table 7.  $ZnFe_2O_4$  exhibits a larger specific surface area than

Table 6  
Specific surface area of  $MFe_2O_4$  using methylene blue test

Adsorbent	$S_{mb}$ ( $m^2/g$ )
$ZnFe_2O_4$	6.2
$CoFe_2O_4$	3.25
50% $CoFe_2O_4$ /50% $ZnFe_2O_4$	6.61

Table 7

Surface area, pore volume, and average pore size for  $MFe_2O_4$  samples before and after methylene blue adsorption

Material	$CoFe_2O_4$		$ZnFe_2O_4$		50% $CoFe_2O_4$ /50% $ZnFe_2O_4$	
	Before	After	Before	After	Before	After
Surface properties						
Pore volume (cc/g)	$2.45 \times 10^{-2}$	0.026	$4.41 \times 10^{-2}$	0.073	$3.22 \times 10^{-2}$	0.043
Surface area ( $m^2/g$ )	71.56	12.08	120.1	17.69	87.54	13.37
Average pore radius (nm)	6.94	1.77	7.38	1.77	7.36	1.63

do  $CoFe_2O_4$  and the composite, which may be attributed to the smaller size of the former.

The surface properties were also determined after MB adsorption (Table 7), and the results showed a large drop in the specific surface area of the adsorbents, confirming the occupation of the adsorbent surface by MB molecules. This decreases the average pore radius and increases the pore volume of the adsorbents.

#### 3.4.2. FTIR analysis

Fig. 8 shows the FTIR spectra of  $MFe_2O_4$ , which confirm the formation and the chemical structure of  $ZnFe_2O_4$ ,  $CoFe_2O_4$ , and the composite. For spinel ferrites, both octahedral and tetrahedral sites are involved in the bonding [51–53]. The absorption bands around  $420 \text{ cm}^{-1}$  are attributed to the vibration mode of  $Fe^{3+}-O^{2-}$  in the tetrahedral sites [43,54] and the absorption bands around  $580 \text{ cm}^{-1}$  are related to the vibration mode of  $Zn^{2+}-O^{2-}$  and  $Co^{2+}-O^{2-}$  in the octahedral sites [40]. The observation of these bands in the spectra of the present samples confirms the successful synthesis of spinel ferrites. Moreover, the bands at  $3,500$  and  $1,600 \text{ cm}^{-1}$  are attributed to the stretching and bending vibration of the O–H group of absorbed water, respectively. As shown in Fig. 8, the bands of the composite are more intense than those of  $CoFe_2O_4$  and  $ZnFe_2O_4$  because it is a combination of two individual spinel ferrites.

Fig. 8 also shows the presence of MB in the spectra of the materials after adsorption, where the peak appearing at  $2,923 \text{ cm}^{-1}$  in the spectra of  $ZnFe_2O_4$  and 50%  $CoFe_2O_4$ /50%

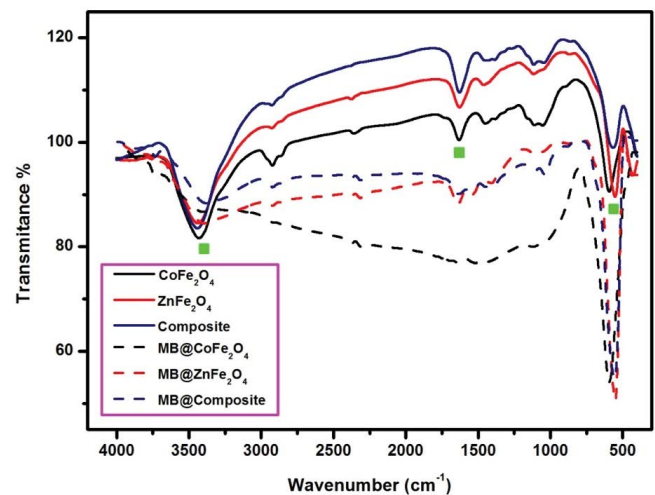


Fig. 8. Fourier transform infrared spectra of  $MFe_2O_4$  before and after methylene blue adsorption.

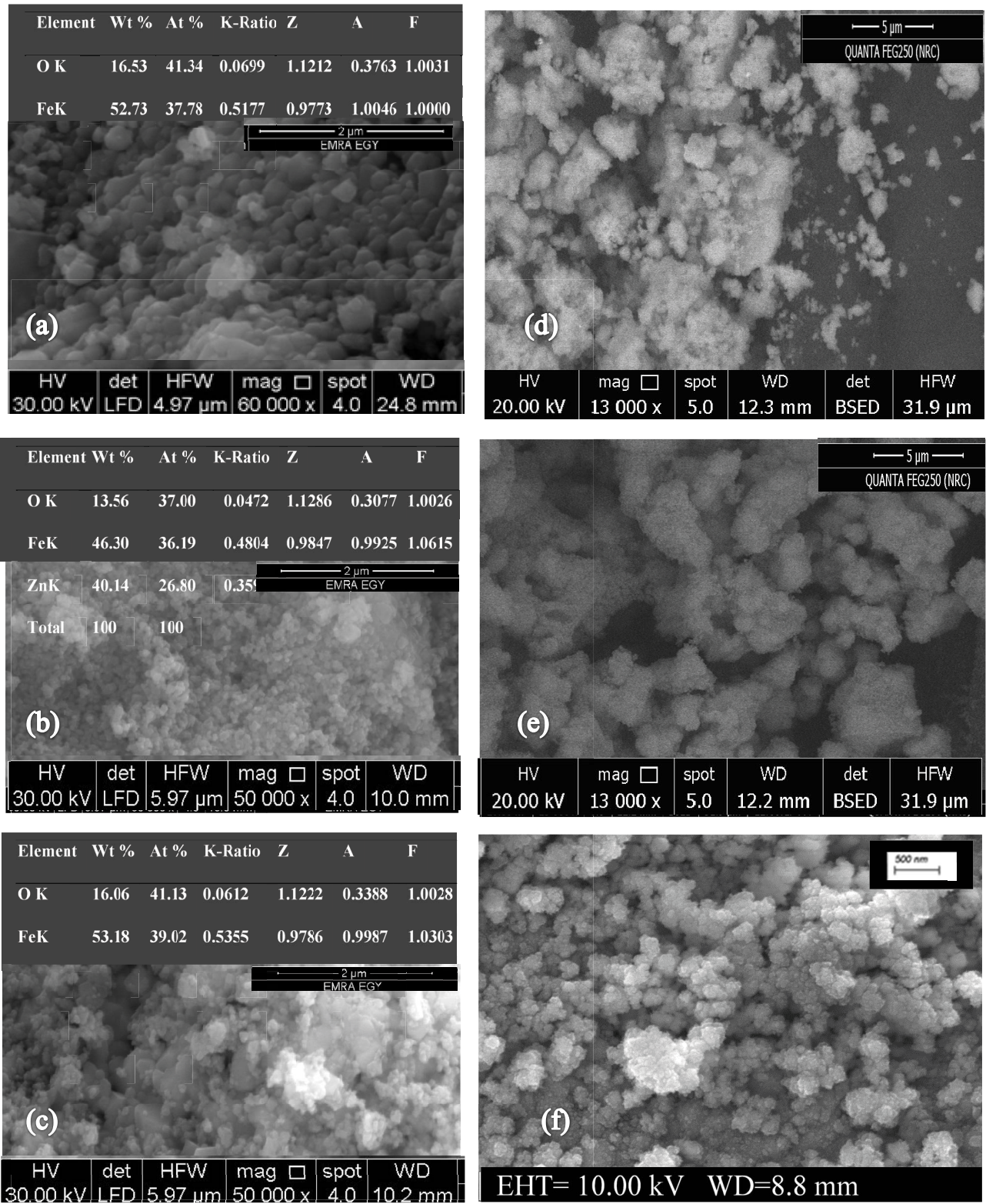


Fig. 9. Field-emission scanning electron microscopy (FESEM) and energy-dispersive X-ray diffraction images of (a) CoFe<sub>2</sub>O<sub>4</sub>, (b) ZnFe<sub>2</sub>O<sub>4</sub>, and (c) 50% CoFe<sub>2</sub>O<sub>4</sub>/50% ZnFe<sub>2</sub>O<sub>4</sub> and FESEM images after methylene blue adsorption of (d) CoFe<sub>2</sub>O<sub>4</sub>, (e) ZnFe<sub>2</sub>O<sub>4</sub>, and (f) 50% CoFe<sub>2</sub>O<sub>4</sub>/50% ZnFe<sub>2</sub>O<sub>4</sub>.

Table 8  
Atomic percentage and weight percentage of  $MFe_2O_4$

Sample	$CoFe_2O_4$			$ZnFe_2O_4$			50% $CoFe_2O_4$ /50% $ZnFe_2O_4$			
	Co	Fe	O	Zn	Fe	O	Co	Zn	Fe	O
Atomic %	20.88	37.78	41.34	26.80	36.19	37	5.87	13.98	39.02	41.13
Weight %	30.75	52.73	16.53	40.14	46.30	13.56	8.45	22.31	53.18	16.06

$ZnFe_2O_4$  can be assigned to the stretching vibration of –CH–aromatic bonds. The characteristics peaks of the aromatic ring structures of MB appear at 1,519 and 1,452  $cm^{-1}$  in the spectrum of  $CoFe_2O_4$ , at 1,544 and 1,409  $cm^{-1}$  in the spectrum of  $ZnFe_2O_4$ , and at 1,409  $cm^{-1}$  in the spectrum of 50%  $CoFe_2O_4$ /50%  $ZnFe_2O_4$  [55]. The peak at 1,108  $cm^{-1}$  in the  $ZnFe_2O_4$  spectrum is attributable to the C=C bonds of the aromatic rings [56]. The decrease in the intensity of these peaks indicates that these bonds are involved in the adsorption process. The bands at 593.1, 552.7, and 556.4  $cm^{-1}$  in the spectra of  $CoFe_2O_4$ ,  $ZnFe_2O_4$ , and 50%  $CoFe_2O_4$ /50%  $ZnFe_2O_4$ , respectively, are due to the –C–H out-of-plane bending vibration of the benzene ring. Fig. 8 shows that most of the peaks intensities (–OH, –C–H, and –NO) change after adsorption, which suggests that the MB molecules form complexes with oxygen-containing functional groups in the ferromagnetic materials.

### 3.4.3. FESEM and EDX

Fig. 9 displays the morphology of the prepared ferrite nanoparticles. As shown in Figs. 9a and b,  $CoFe_2O_4$  has a hexagonal shape, whereas  $ZnFe_2O_4$  exhibits a uniform spherical morphology. The two phases can be clearly observed in Fig. 9c. Owing to the difference in size and shape between  $CoFe_2O_4$  and  $ZnFe_2O_4$ , the spherical particles of the latter decorate the surface of the former.

Figs. 9d–f shows that the surfaces of the adsorbents are covered with a layer of the dye and the surfaces become less uniform after MB adsorption. This suggests that the MB adsorption onto  $MFe_2O_4$  could proceed via physical adsorption or surface precipitation.

An EDX analysis was performed to examine the purity and chemical composition of the prepared samples, and the corresponding micrographs are shown in Figs. 9a–c. All peaks are in accord with the standard positions, which confirms the expected stoichiometry.

The data summarized in Table 8 reveals that all precursors underwent a chemical reaction to form ferrite materials of the expected composition.

According to the results of the effect of pH, adsorption isotherms, and FTIR analyses, it can be concluded that the MB adsorption onto the materials under study proceeds through a mechanism involving electrostatic adsorption and complexation via  $\pi$ – $\pi$  interaction. Moreover, the  $N_2$  adsorption and kinetic studies suggest intraparticle diffusion as a probable mechanism.

## 4. Conclusion

With the aim of developing new adsorbents for the removal of pollutants, we have synthesized magnetic,

highly porous nanoparticles of formula  $MFe_2O_4$  ( $M = Co, Zn, \text{ and } 50\% \text{ Co}/50\% \text{ Zn}$ ) and evaluated their performance in the adsorption of MB. It was concluded that factors like the preparation condition of the nanoparticles and their dose, the pH of the adsorption solution, and the initial concentration of the model dye play important roles in the adsorption process, which is favored in alkaline media and at high MB initial concentration. The kinetic results showed that the adsorption onto  $MFe_2O_4$  nanoparticles followed pseudo-second-order and intraparticle diffusion models.

## Acknowledgments

The authors are grateful to EKB (Egyptian Knowledge Bank) for its kind support for language editing service through ENAGO.

## References

- [1] N. Barka, M. Abdennouri, M.E.L. Makhfouk, Removal of Methylene Blue and Eriochrome Black T from aqueous solutions by biosorption on *Scolymus hispanicus* L.: kinetics, equilibrium and thermodynamics, *J. Taiwan Inst. Chem. Eng.*, 42 (2011) 320–326.
- [2] M.M. El-Rabie, A.A. Farghali, N.H. Mahmoud, N. Shehata, M.M. Faisle, Evaluation of carbon nanotubes (CNTs) in management of a full scale centralized wastewater treatment plant, *Res. J. Pharm. Biol. Chem. Sci.*, 8 (2017) 1180–1190.
- [3] A.B. Albadarin, M.N. Collins, M. Naushad, S. Shirazian, G. Walker, C. Mangwandi, Activated lignin-chitosan extruded blends for efficient adsorption of methylene blue, *Chem. Eng. J.*, 307 (2017) 264–272.
- [4] A.A. Alqadami, M. Naushad, Z.A. AlOthman, T. Ahamad, Adsorptive performance of MOF nanocomposite for methylene blue and malachite green dyes: kinetics, isotherm and mechanism, *J. Environ. Manage.*, 223 (2018) 29–36.
- [5] M. Naushad, A.A. Alqadami, Z.A. AlOthman, I.H. Alshaimi, M.S. Algamdi, A.M. Aldawsari, Adsorption kinetics, isotherm and reusability studies for the removal of cationic dye from aqueous medium using arginine modified activated carbon, *J. Mol. Liq.*, 293 (2019) 1–8, doi: 10.1016/j.molliq.2019.111442.
- [6] J. Mohanraj, D. Durgalakshmi, S. Balakumar, P. Aruna, S. Ganesan, S. Rajendran, M. Naushad, Low cost and quick time absorption of organic dye pollutants under ambient condition using partially exfoliated graphite, *J. Water Process Eng.*, 34 (2020) 1–8, doi: 10.1016/j.jwpe.2019.101078.
- [7] D.N. Ahmed, L.A. Najj, A.A.H. Faisal, N. Al-Ansari, M. Naushad, Waste foundry sand/MgFe-layered double hydroxides composite material for efficient removal of Congo red dye from aqueous solution, *Sci. Rep.*, 10 (2020) 1–12.
- [8] R. Rahimi, H. Kerdari, M. Rabbani, M. Shafiee, Synthesis, characterization and adsorbing properties of hollow  $Zn-Fe_2O_4$  nanospheres on removal of Congo red from aqueous solution, *Desalination*, 280 (2011) 412–418.
- [9] T. Etemadinia, A. Allahrasani, B. Barikbin,  $ZnFe_2O_4@SiO_2@Tragacanth$  gum nanocomposite: synthesis and its application for the removal of methylene blue dye from aqueous solution, *Polym. Bull.*, 76 (2019) 6089–6109.

- [10] X. Hou, J. Feng, X. Liu, Y. Ren, Z. Fan, M. Zhang, Magnetic and high rate adsorption properties of porous  $Mn_{1-x}Zn_xFe_2O_4$  ( $0 \leq x \leq 0.8$ ) adsorbents, *J. Colloid Interface Sci.*, 353 (2011) 524–529.
- [11] J. Li, D.H.L. Ng, P. Song, Y. Song, C. Kong, Bio-inspired synthesis and characterization of mesoporous  $ZnFe_2O_4$  hollow fibers with enhancement of adsorption capacity for acid dye, *J. Ind. Eng. Chem.*, 23 (2015) 290–298.
- [12] W. Konicki, D. Sibera, E. Mijowska, Z. Lendzion-Bieluś, U. Narkiewicz, Equilibrium and kinetic studies on acid dye Acid Red 88 adsorption by magnetic  $ZnFe_2O_4$  spinel ferrite nanoparticles, *J. Colloid Interface Sci.*, 398 (2013) 152–160.
- [13] J. Feng, Y. Wang, L. Zou, B. Li, X. He, Y. Ren, Y. Lv, Z. Fan, Synthesis of magnetic  $ZnO/ZnFe_2O_4$  by a microwave combustion method, and its high rate of adsorption of methylene blue, *J. Colloid Interface Sci.*, 438 (2015) 318–322.
- [14] Y.D. Liang, Y.J. He, T.T. Wang, L.H. Lei, Adsorptive removal of gentian violet from aqueous solution using  $CoFe_2O_4$ /activated carbon magnetic composite, *J. Water Process Eng.*, 27 (2019) 77–88.
- [15] J. Xu, P. Xin, Y. Gao, B. Hong, H. Jin, D. Jin, X. Peng, J. Li, J. Gong, H. Ge, Magnetic properties and methylene blue adsorptive performance of  $CoFe_2O_4$ /activated carbon nanocomposites, *Mater. Chem. Phys.*, 147 (2014) 915–919.
- [16] T. Tatarchuk, N. Paliychuk, R.B. Bitra, A. Shyichuk, M. Naushad, I. Mironyuk, D. Ziolkowska, Adsorptive removal of toxic Methylene Blue and Acid Orange 7 dyes from aqueous medium using cobalt-zinc ferrite nano-adsorbents, *Desal. Water Treat.*, 150 (2019) 374–385.
- [17] L. Ai, Y. Zhou, J. Jiang, Removal of methylene blue from aqueous solution by montmorillonite/ $CoFe_2O_4$  composite with magnetic separation performance, *Desalination*, 266 (2011) 72–77.
- [18] P. Samoila, C. Cojocar, I. Cretescu, C.D. Stan, V. Nica, L. Sacarescu, V. Harabagiu, Nanosized spinel ferrites synthesized by sol-gel autocombustion for optimized removal of azo dye from aqueous solution, *J. Nanomater.*, 16 (2015) 237.
- [19] Z. Ding, W. Wang, Y. Zhang, F. Li, J.P. Liu, Synthesis, characterization and adsorption capability for Congo red of  $CoFe_2O_4$  ferrite nanoparticles, *J. Alloys Compd.*, 640 (2015) 362–370.
- [20] X. Zhao, W. Wang, Y. Zhang, S. Wu, F. Li, J.P. Liu, Synthesis and characterization of gadolinium doped cobalt ferrite nanoparticles with enhanced adsorption capability for Congo Red, *Chem. Eng. J.*, 250 (2014) 164–174.
- [21] S. Yavari, N.M. Mahmodi, P. Teymouri, B. Shahmoradi, A. Maleki, Cobalt ferrite nanoparticles: preparation, characterization and anionic dye removal capability, *J. Taiwan Inst. Chem. Eng.*, 59 (2016) 320–329.
- [22] N.M. Jacob, P. Kuruva, G. Madras, T. Thomas, Purifying water containing both anionic and cationic species using a (Zn, Cu) O, ZnO, and cobalt ferrite based multiphase adsorbent system, *Ind. Eng. Chem. Res.*, 52 (2013) 16384–16395.
- [23] N. Li, M. Zheng, X. Chang, G. Ji, H. Lu, L. Xue, L. Pan, J. Cao, Preparation of magnetic  $CoFe_2O_4$ -functionalized graphene sheets via a facile hydrothermal method and their adsorption properties, *J. Solid State Chem.*, 184 (2011) 953–958.
- [24] O.A. Oyetade, V.O. Nyamori, B.S. Martincigh, S.B. Jonnalagadda, Effectiveness of carbon nanotube-cobalt ferrite nanocomposites for the adsorption of rhodamine B from aqueous solutions, *RSC Adv.*, 5 (2015) 22724–22739.
- [25] L. Wang, J. Li, Y. Wang, L. Zhao, Q. Jiang, Adsorption capability for Congo red on nanocrystalline  $MFe_2O_4$  ( $M = Mn, Fe, Co, Ni$ ) spinel ferrites, *Chem. Eng. J.*, 181 (2012) 72–79.
- [26] P. Zhang, I. Lo, D. O'Connor, S. Pehkonen, H. Cheng, D. Hou, High efficiency removal of methylene blue using SDS surface-modified  $ZnFe_2O_4$  nanoparticles, *J. Colloid Interface Sci.*, 508 (2017) 39–48.
- [27] J.C. Xu, P.H. Xin, Y.B. Han, P.F. Wang, H.X. Jin, D.F. Jin, X.L. Peng, B. Hong, J. Li, H.L. Ge, Magnetic response and adsorptive properties for methylene blue of  $CoFe_2O_4/Co_3Fe_4$ /activated carbon magnetic composites, *J. Alloys Compd.*, 617 (2014) 622–626.
- [28] T. Tatarchuk, N. Paliychuk, Adsorption of methylene blue onto  $CoFe_2O_4$  spinel ferrite nanoparticles, (2016).
- [29] A.C. Nkele, U.K. Chime, A.C. Nwanya, D. Obi, R.U. Osuji, R. Bucher, P.M. Ejikeme, M. Maaza, F.I. Ezema, Role of metallic dopants on the properties of copper (I) iodide nanopod-like structures, *Vaccum*, 161 (2019) 306–313.
- [30] M.S. El-Geundi, E.A. Ashour, R.M.A. Abobeah, N. Shehata, Determination of specific surface area of natural clay by comparative methods, *Int. J. Sci. Eng. Technol. Res.*, 3 (2014) 2100–2104.
- [31] T. Liu, Y. Li, Q. Du, J. Sun, Y. Jiao, G. Yang, Z. Wang, Y. Xia, W. Zhang, K. Wang, Adsorption of methylene blue from aqueous solution by graphene, *Colloids Surf., B*, 90 (2012) 197–203.
- [32] I. Langmuir, The constitution and fundamental properties of solids and liquids. Part I. Solids, *J. Am. Chem. Soc.*, 38 (1916) 2221–2295.
- [33] H.M.F. Freundlich, Over the adsorption in solution, *J. Phys. Chem.*, 57 (1906) 1100–1107.
- [34] M. Lin, Z. Zhao, F. Cui, S. Xia, Modeling of equilibrium and kinetics of chlorobenzene (CB) adsorption onto powdered activated carbon (PAC) for drinking water treatment, *Desal. Water Treat.*, 44 (2012) 245–254.
- [35] S. Azizian, Kinetic models of sorption: a theoretical analysis, *J. Colloid Interface Sci.*, 276 (2004) 47–52.
- [36] Y.S. Ho, G. McKay, Pseudo-second order model for sorption processes, *Process Biochem.*, 34 (1999) 451–465.
- [37] W. Plazinski, W. Rudzinski, Kinetics of adsorption at solid/solution interfaces controlled by intraparticle diffusion: a theoretical analysis, *J. Phys. Chem. C*, 113 (2009) 12495–12501.
- [38] N. Song, S. Gu, Q. Wu, C. Li, J. Zhou, P. Zhang, W. Wang, M. Yue, Facile synthesis and high-frequency performance of  $CoFe_2O_4$  nanocubes with different size, *J. Magn. Magn. Mater.*, 451 (2018) 793–798.
- [39] G. Qi, H. Ren, H. Fan, Y. Liu, Preparation of  $CoFe_2O_4$  nanoparticles based on high-gravity technology and application for the removal of lead, *Chem. Eng. Res. Des.*, 147 (2019) 520–528.
- [40] X. Huang, Y. Qin, Y. Ma, Y. Chen, Preparation and electromagnetic properties of nanosized  $ZnFe_2O_4$  with various shapes, *Ceram. Int.*, 45 (2019) 18389–18397.
- [41] R. Hoppe, G. Alberti, U. Costantino, C. Dionigi, G. Schulz-Ekloff, R. Vivani, Intercalation of dyes in layered zirconium phosphates. 1. Preparation and spectroscopic characterization of  $\alpha$ -zirconium phosphate crystal violet compounds, *Langmuir*, 13 (1997) 7252–7257.
- [42] J. Garcia-Martín, R. López-Garzón, M.L. Godino-Salido, M.D. Gutiérrez-Valero, P. Arranz-Mascarós, R. Cuesta, F. Carrasco-Marín, Ligand adsorption on an activated carbon for the removal of chromate ions from aqueous solutions, *Langmuir*, 21 (2005) 6908–6914.
- [43] E. Ferdosi, H. Bahiraei, D. Ghanbari, Investigation the photocatalytic activity of  $CoFe_2O_4/ZnO$  and  $CoFe_2O_4/ZnO/Ag$  nanocomposites for purification of dye pollutants, *Sep. Purif. Technol.*, 211 (2019) 35–39.
- [44] J.R. Kim, B. Santiano, H. Kim, E. Kan, Heterogeneous oxidation of methylene blue with surface-modified iron-amended activated carbon, *Am. J. Anal. Chem.*, 4 (2013) 115–122.
- [45] X. Hou, J. Feng, Y. Ren, Z. Fan, M. Zhang, Synthesis and adsorption properties of spongelike porous  $MnFe_2O_4$ , *Colloids Surf., A*, 363 (2010) 1–7.
- [46] X. Hou, J. Feng, X. Liu, Y. Ren, Z. Fan, T. Wei, J. Meng, M. Zhang, Synthesis of 3D porous ferromagnetic  $NiFe_2O_4$  and using as novel adsorbent to treat wastewater, *J. Colloid Interface Sci.*, 362 (2011) 477–485.
- [47] L. Yang, Y. Zhang, X. Liu, X. Jiang, Z. Zhang, T. Zhang, L. Zhang, The investigation of synergistic and competitive interaction between dye Congo red and methyl blue on magnetic  $MnFe_2O_4$ , *Chem. Eng. J.*, 246 (2014) 88–96.
- [48] Z. Gao, F. Cui, S. Zeng, L. Guo, J. Shi, A high surface area superparamagnetic mesoporous spinel ferrite synthesized by a template-free approach and its adsorptive property, *Microporous Mesoporous Mater.*, 132 (2010) 188–195.

- [49] X. Han, P. Tian, H. Pang, Q. Song, G. Ning, Y. Yu, H. Fang, Facile synthesis of magnetic hierarchical MgO–MgFe<sub>2</sub>O<sub>4</sub> composites and their adsorption performance towards Congo red, *Rsc Adv.*, 4 (2014) 28119–28125.
- [50] J. Zhang, J.M. Song, H.L. Niu, C.J. Mao, S.Y. Zhang, Y.H. Shen, ZnFe<sub>2</sub>O<sub>4</sub> nanoparticles: synthesis, characterization, and enhanced gas sensing property for acetone, *Sens. Actuators, B*, 221 (2015) 55–62.
- [51] B.J. Rani, M. Ravina, B. Saravanakumar, G. Ravi, V. Ganesh, S. Ravichandran, R. Yuvakkumar, Ferrimagnetism in cobalt ferrite (CoFe<sub>2</sub>O<sub>4</sub>) nanoparticles, *Nanostruct. Nano-Objects*, 14 (2018) 84–91.
- [52] M. Qasim, K. Asghar, D. Das, Preparation and characterization of CoFe<sub>2</sub>O<sub>4</sub> and CoFe<sub>2</sub>O<sub>4</sub>@Albumen nanoparticles for biomedical applications, *Ceram. Int.*, 45 (2019) 24971–24981.
- [53] V.H. Ojha, K.M. Kant, Temperature dependent magnetic properties of superparamagnetic CoFe<sub>2</sub>O<sub>4</sub> nanoparticles, *Physica B*, 567 (2019) 87–94.
- [54] X. Zhang, Z. Chen, C. Wu, J. Zhang, F. Wang, Solvothermal synthesis of spinel ZnFe<sub>2</sub>O<sub>4</sub> nanoparticles with enhanced infrared radiation property, *Chem. Phys. Lett.*, 732 (2019) 1–7, doi: 10.1016/j.cplett.2019.136647.
- [55] Y.Y. Lau, Y.S. Wong, T.T. Teng, N. Morad, M. Rafatullah, S.A. Ong, Degradation of cationic and anionic dyes in coagulation–flocculation process using bi-functionalized silica hybrid with aluminum–ferric as auxiliary agent, *RSC Adv.*, 5 (2015) 34206–34215.
- [56] A.C. Pradhan, A. Paul, G.R. Rao, Sol-gel-cum-hydrothermal synthesis of mesoporous Co-Fe@Al<sub>2</sub>O<sub>3</sub>-MCM-41 for methylene blue remediation, *J. Chem. Sci.*, 129 (2017) 381–395.

### Supplementary information

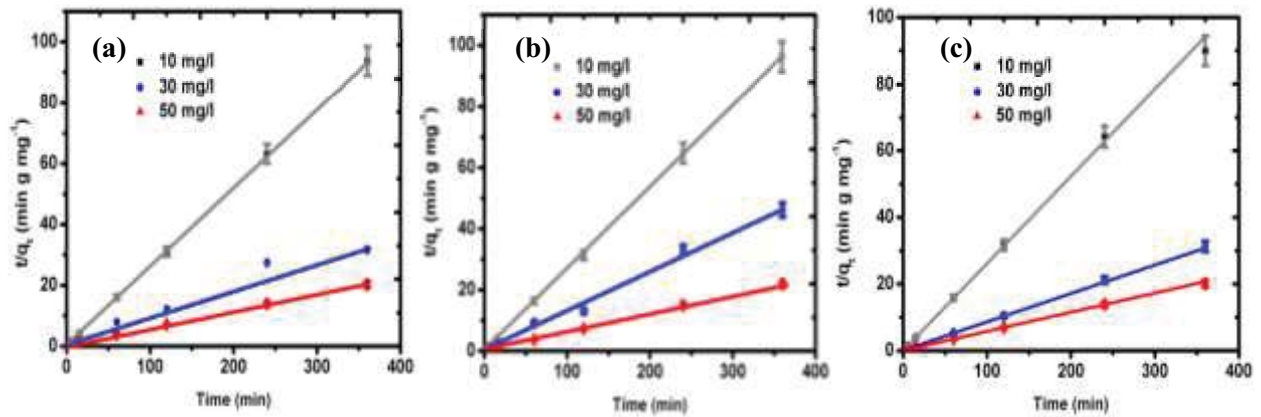


Fig. S1. Pseudo-first-order model for the adsorption of MB at different concentrations onto ZnFe<sub>2</sub>O<sub>4</sub> (a), CoFe<sub>2</sub>O<sub>4</sub> (b) and 50% CoFe<sub>2</sub>O<sub>4</sub>+50% ZnFe<sub>2</sub>O<sub>4</sub> (c).

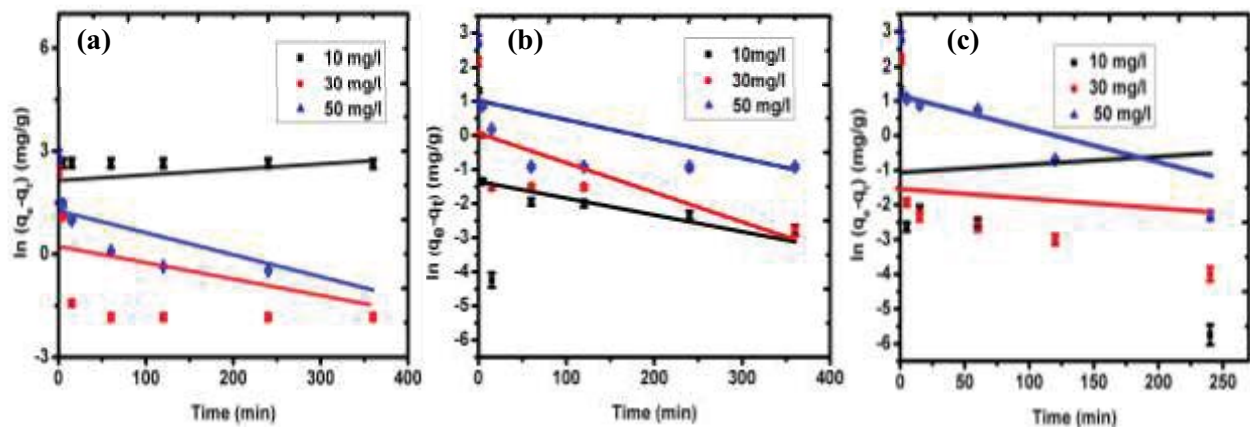


Fig. S2. Pseudo-second-order model for the adsorption of MB at different concentrations onto ZnFe<sub>2</sub>O<sub>4</sub> (a), CoFe<sub>2</sub>O<sub>4</sub> (b), and 50% CoFe<sub>2</sub>O<sub>4</sub>+50% ZnFe<sub>2</sub>O<sub>4</sub> (c).

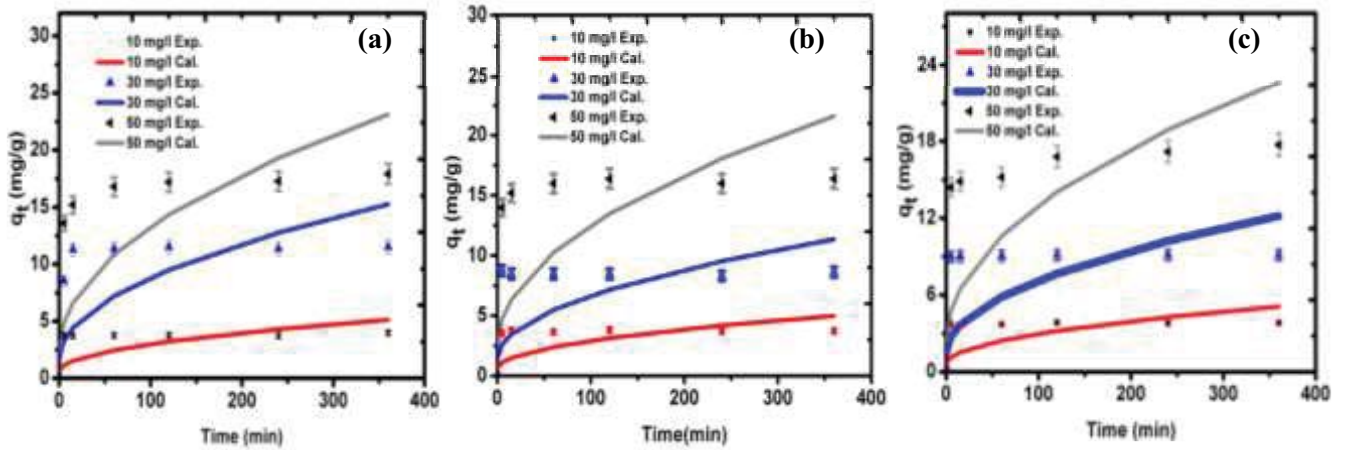


Fig. S3. Intraparticle diffusion kinetic models for the adsorption of MB at different concentrations onto  $ZnFe_2O_4$  (a),  $CoFe_2O_4$  (b), and 50%  $CoFe_2O_4$ +50%  $ZnFe_2O_4$  (c).

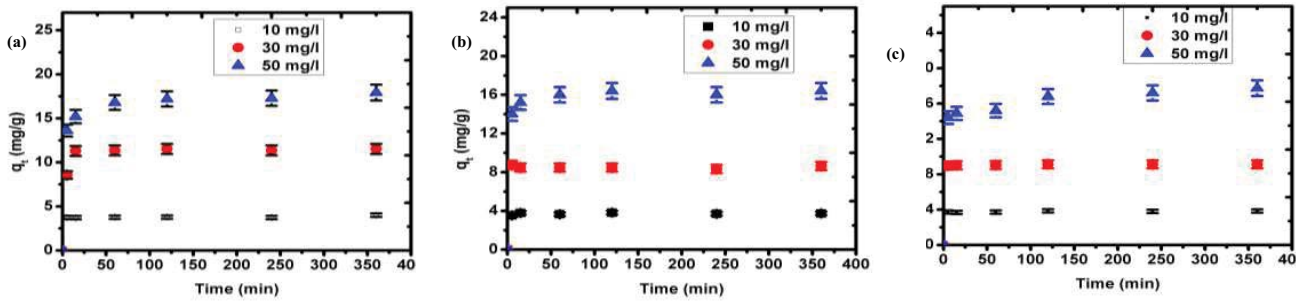


Fig. S4. Kinetic curve for the adsorption of MB at different concentrations onto  $ZnFe_2O_4$  (a),  $CoFe_2O_4$  (b), 50%  $CoFe_2O_4$  + 50%  $ZnFe_2O_4$  (c).